JACS
JOURNAL OF THE AMERICAN CHEMICAL SOCIETY
Article
pubs.acs.org/JACS

Redox Chemistries and Plasmon Energies of Photodoped In_2O_3 and Sn-Doped In_2O_3 (ITO) Nanocrystals

Alina M. Schimpf,[†] Sebastien D. Lounis,[‡,§] Evan L. Runnerstrom,[§,∥,⊥] Delia J. Milliron,*[,§,⊥] and Daniel R. Gamelin*[,†]

[†]Department of Chemistry, University of Washington, Seattle, Washington 98195-1700, United States
[‡]Graduate Group in Applied Science & Technology and [∥]Department of Materials Science and Engineering, University of California, Berkeley, Berkeley, California 94720, United States
[§]The Molecular Foundry, Lawrence Berkeley National Laboratory, Berkeley, CA 94720, United States
[⊥]McKetta Department of Chemical Engineering, The University of Texas at Austin, Austin, Texas 78712, United States

Supporting Information

ABSTRACT: Plasmonic doped semiconductor nanocrystals promise exciting opportunities for new technologies, but basic features of the relationships between their structures, compositions, electronic structures, and optical properties remain poorly understood. Here, we report a quantitative assessment of the impact of composition on the energies of localized surface plasmon resonances (LSPRs) in colloidal tin-doped indium oxide ($Sn:In_2O_3$, or ITO) nanocrystals. Using a combination of aliovalent doping and photodoping, the effects of added electrons and impurity ions on the energies of LSPRs in colloidal In_2O_3 and ITO nanocrystals have been evaluated. Photodoping allows electron densities to be tuned post-synthetically in ITO nanocrystals, independent of their Sn content. Because electrons added photochemically are easily titrated, photodoping also allows independent quantitative determination of the dependence of the LSPR energy on nanocrystal composition and changes in electron density. The data show that ITO LSPR energies are affected by both electron and Sn concentrations, with composition yielding a broader plasmon tuning range than achievable by tuning carrier densities alone. Aspects of the photodoping energetics, as well as magneto-optical properties of these ITO LSPRs, are also discussed.

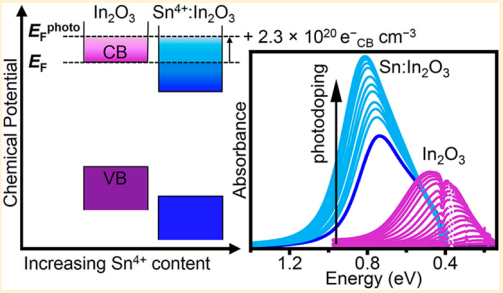

INTRODUCTION

Localized surface plasmon resonances (LSPRs) in semiconductor nanocrystals have recently attracted broad attention,[1−6] in part because of their tunability in both energy and intensity via tunable carrier densities. Charge-carrier densities in semiconductor nanocrystals have been modulated by various techniques including remote doping,[7−13] vacancy generation,[14−17] aliovalent doping,[18−25] electrochemical doping,[26−29] and photodoping,[8,21,28,30−40] each offering specific advantages. For example, aliovalently doped colloidal nanocrystals such as Sn-doped In_2O_3 (ITO)[18,19,41−44] and Al-doped ZnO (AZO)[20,21,45] contain conduction-band electrons that are stable in air, making them attractive for potential aerobic applications. Alternatively, photodoped ZnO nanocrystals contain reactive conduction-band electrons that can be readily titrated against mild oxidants,[21,31,33,38] making the carrier densities associated with their LSPRs directly quantifiable.[46] The reactivities of these electrons also provide opportunities for fundamental studies of interfacial electron-transfer reactions involving semiconductor nanostructures.[10,11,36,37,47]

Characterization of the electronic structures of doped semiconductor nanocrystals poses interesting challenges. For example, using photodoped ZnO nanocrystals, we have recently observed that the LSPR energies of doped semiconductors are strongly coupled to the one-electron intraband transition energies, causing divergence from the classical Drude model when in the quantum confinement size regime.[46] A second potentially important feature of doped nanocrystal electronic structure that has not received sufficient attention in LSPR analyses is the impact of the sizable electronic-structural changes that frequently accompany the introduction of lattice defects (e.g., impurities, vacancies) even in the absence of free carriers. Such effects are widely discussed in the context of band gap engineering[36,48,49] but have not been thoroughly explored for the purposes of plasmon engineering in semiconductor nanocrystals. For example, isovalent Mg^{2+} doping is known to shift the potentials of extra conduction-band electrons in *n*-type $Zn_{1-x}Mg_xO$ nanocrystals,[36] and it would be reasonable to expect that it might also tune LSPR energies. Although LSPRs in $Cu_{2-x}E$ (E = S, Se, Te) nanocrystals are generally attributed to formation of nonstoichiometric compositions,[14,16,50] the impact of the compositional changes alone on LSPR energies has not been addressed. Typically, these ancillary compositional

Received: November 13, 2014
Published: December 9, 2014

DOI: 10.1021/ja5116953
J. Am. Chem. Soc. 2015, 137, 518−524

changes are difficult to disentangle from the effects of changing free-carrier density, and to our knowledge, this issue has not been previously addressed for any plasmonic semiconductor nanocrystals.

Here, we use a combination of aliovalent doping and photodoping to separately evaluate the effects of added electrons and impurity ions on the LSPR energies in In_2O_3-based nanocrystals. We demonstrate controlled photodoping of both In_2O_3 and ITO nanocrystals using EtOH as a sacrificial reductant. The added conduction-band electrons can be titrated using mild oxidants, allowing them to be quantified without reliance on modeling of absorption energies and bandshapes based on the Drude approximation or Mie theory. The results reveal that the LSPR energies are affected separately by both electron and Sn concentrations, with compositional engineering offering a greater range in LSPR energies than can be achieved by tuning carrier densities alone. Surprisingly, the maximum number of electrons that can be added photochemically is independent of the number of electrons already present due to Sn doping, providing general insight into the factors governing nanocrystal photodoping. Finally, magnetic circular dichroism (MCD) spectroscopy of the ITO LSPR reveals properties similar to those of metal nanoparticles and heavily *n*-doped ZnO nanocrystals. The large magneto-optical responses from the IR LSPRs of doped semiconductor nanocrystals may have interesting ramifications for applications such as IR chiral imaging or sensing.

RESULTS AND ANALYSIS

In_2O_3 and ITO nanocrystals were synthesized as described previously.[43] Absorption spectra of all samples are provided as Supporting Information (Figure S1). In_2O_3 and ITO nanocrystals were photodoped in the same manner as detailed[32,33,38] for ZnO nanocrystals (see Experimental Methods). Specifically, exposure to UV illumination under rigorously anaerobic conditions and in the presence of a sacrificial reductant (EtOH) leads to the accumulation of conduction-band electrons (Figure 1, top). Photodoping is evident from the appearance and growth of a new IR absorption band in the case of In_2O_3 nanocrystals and from an increase and blue shift of the existing IR absorption band in the case of ITO nanocrystals (Figure 1, bottom). Note that the new IR absorption resulting from ITO photodoping has a similar energy and band shape as the IR absorption of the as-prepared ITO nanocrystals. As observed with ZnO nanocrystals,[33,38] a maximum photodoping level is approached asymptotically under these conditions (see Experimental Methods). Importantly, this photodoping is completely reversible, with the In_2O_3 and ITO nanocrystals returning to their as-prepared state upon exposure to air or other mild oxidants.

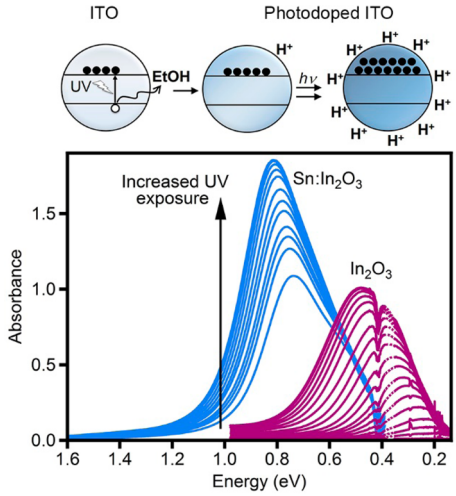

Figure 1. Top: Scheme depicting photodoping of In_2O_3 and ITO nanocrystals. Bottom: Absorption spectra before and following various extents of photodoping of In_2O_3 (right, ~0.4 eV) and 9.0% Sn-doped In_2O_3 (left, ~0.8 eV) nanocrystals (~20 μM in 7:1 toluene/EtOH). The arrows show the direction of increasing photodoping.

The reversibility of this photodoping allows the number of photogenerated electrons to be counted via oxidative titration.[21,31,33,37,38,46] Oxidants such as air or $[FeCp^*_2]^+$ remove the electrons (eq 1) added photochemically but have no effect on those arising from Sn doping, indicating greater stability of the latter. Using stronger oxidants such as Ce^{4+}, $[NO]^+$, or $[N(C_6H_4Br\text{-}4)_3]^{\bullet+}$, roughly half of the remaining ITO electrons could be removed (Figure S2), but this chemistry leads to nanocrystal precipitation. Nevertheless, this result confirms the greater chemical stability of electrons generated via aliovalent doping than of those added photochemically, despite their spectroscopic similarity (Figure 1). Greater stability of electrons added via aliovalent doping over photochemically added ones is also observed in ZnO nanocrystals.[21]

$$e^-_{CB}{:}NC + [FeCp^*_2]^+ \rightarrow NC + FeCp^*_2 \quad (1)$$

$$NC = In_2O_3 \text{ or ITO nanocrystal}$$

Figure 2a shows infrared absorption spectra of photodoped 5.9% Sn:In_2O_3 nanocrystals as a function of added titrant. Addition of $[FeCp^*_2]^+$ to the maximally photodoped nanocrystals (top, solid blue) decreases the LSPR intensity (dotted green) until the spectrum of the as-prepared ITO nanocrystals is recovered (solid purple). The inset of Figure 2a plots the integrated absorption intensity versus equivalents of $[FeCp^*_2]^+$. The solid line is a linear fit to the data. These intensities are normalized such that the as-prepared nanocrystals have a relative integrated absorbance of 1.0. The intersection of the fitted line with 1.0 thus defines the average number of electrons per nanocrystal added photochemically ($\langle n_{photo} \rangle$). Furthermore, extrapolation of this line to zero absorption represents the average total number of electrons present in the maximally photodoped nanocrystals ($\langle n_{tot} \rangle$). The difference, $\langle n_{tot} \rangle - \langle n_{photo} \rangle$, describes the number of electrons initially present in the as-prepared ITO nanocrystals ($\langle n_{as\text{-}prepared} \rangle$). For the sample of Figure 2a, this analysis yields $\langle n_{photo} \rangle = 28$, $\langle n_{as\text{-}prepared} \rangle = 46$, and $\langle n_{tot} \rangle = 74$. We note that this extrapolation may underestimate $\langle n_{as\text{-}prepared} \rangle$ because the plasmon intensity is only linear with $\langle n \rangle$ when integrating over the entire spectrum, and the data in Figure 2a are limited by solvent absorption and the spectrometer sensitivity window (see Experimental Methods for details). Fortunately, the spectra of samples with large $\langle n_{as\text{-}prepared} \rangle$ can be mostly integrated (e.g., Figure 2a), and the spectra that cannot be as completely measured come from samples with smaller values of $\langle n_{as\text{-}prepared} \rangle$ that require less extrapolation.

To probe the role of Sn, samples of ITO nanocrystals with Sn contents ranging from 0.0–9.0% were each photodoped to the maximum extent, and then their electrons were titrated as described above. To correct for volume effects,[38] the resulting data are presented as average electron densities, $\langle N \rangle$. Figure 2b

DOI: 10.1021/ja5116953
J. Am. Chem. Soc. 2015, 137, 518–524

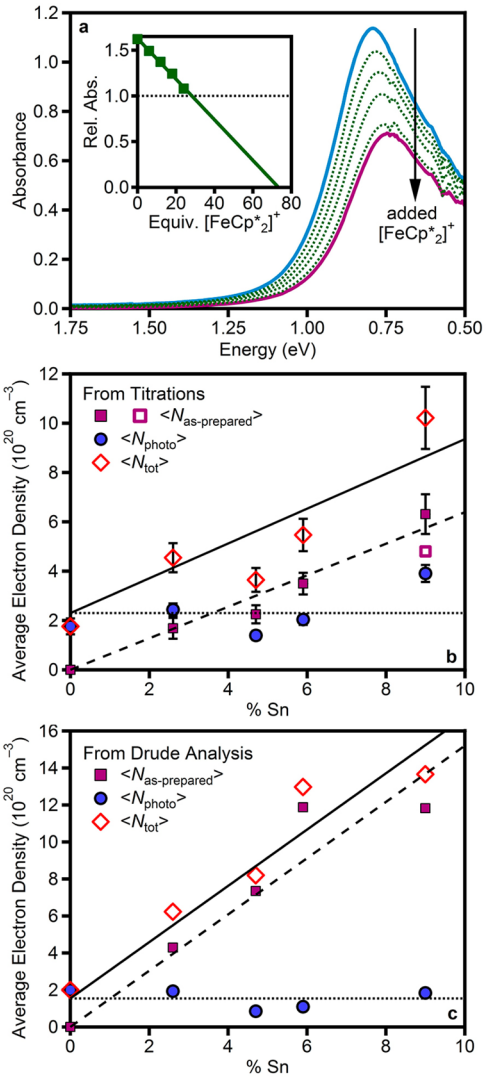

Figure 2. (a) Absorption spectra of as-prepared (bottom, purple) and maximally photodoped (top, blue) 5.9% Sn:In_2O_3 nanocrystals (0.6 μM in 1:1 toluene/THF with 3×10^5 equiv EtOH). The intermediate spectra (dotted, green) were measured after adding various amounts of $[FeCp^*_2][BAr_F]$ to the maximally photodoped nanocrystals. The arrow indicates increasing $[FeCp^*_2][BAr_F]$. Inset: Relative integrated IR absorption as a function of added $[FeCp^*_2][BAr_F]$. The solid line is a linear fit to the data. The crossing of this line with 1.0 yields $\langle n_{photo} \rangle$, the intercept with 0.0 yields $\langle n_{tot} \rangle$, and the difference between $\langle n_{photo} \rangle$ and $\langle n_{tot} \rangle$ yields $\langle n_{as\text{-}prepared} \rangle$. (b,c) Electron densities, $\langle N_{as\text{-}prepared} \rangle$ (squares), $\langle N_{photo} \rangle$ (circles), and $\langle N_{tot} \rangle$ (diamonds) obtained from titrations and Drude analysis, respectively, plotted versus nanocrystal Sn content. The lines are guides to the eye, fitted such that $\langle N_{tot} \rangle = \langle N_{as\text{-}prepared} \rangle + \langle N_{photo} \rangle$ across the range of Sn content. The error bars in the experimental data were determined from multiple titrations on each sample and from error bars in the quantitative concentration measurements.

plots the electron densities, $\langle N_{as\text{-}prepared} \rangle$, $\langle N_{photo} \rangle$, and $\langle N_{tot} \rangle$ as a function of Sn concentration. $\langle N_{as\text{-}prepared} \rangle$ increases rougly linearly from the origin as the Sn content increases, consistent with the role of Sn as an *n*-type dopant. Figure 2b shows that $\langle N_{tot} \rangle$ also increases linearly with increasing Sn content, but no longer starts at zero for 0% Sn. Quite unexpectedly, $\langle N_{photo} \rangle$ is almost completely insensitive to Sn concentration and is therefore essentially independent of $\langle N_{as\text{-}prepared} \rangle$. Averaging over all samples yields $\langle \langle N_{photo} \rangle \rangle = 2.3 \pm 0.8 \times 10^{20}$ cm^{-3}. This value is slightly higher than that found for ZnO nanocrystals photodoped under the same conditions ($1.4 \pm 0.4 \times 10^{20}$ cm^{-3}).[38]

These titrations determine carrier densities without relying on a model-dependent analysis of LSPR energies, which presents an opportunity for critical comparison with use of the extended Drude model to analyze carrier concentrations in ITO nanocrystals based on LSPR spectra.[43,51,52] Spectra of the as-prepared ITO and all the photodoped nanocrystals were fit using a parametrized dielectric function that included a frequency-dependent damping function, as typically found for ITO.[53−55] The extracted electron densities $\langle N_{as\text{-}prepared} \rangle$ and $\langle N_{tot} \rangle$ trend monotonically and approximately linearly upward with Sn content (Figure 2c). Notably, for photodoped In_2O_3 quantitative agreement is found between the titration-derived $\langle N_{photo} \rangle$ and the value determined by fitting. In addition, $\langle N_{photo} \rangle$ is found to have a constant value across Sn content, consistent with the results of the titration. Hence, the trends in carrier densities determined by the model-free titration approach and analysis based on fitting to the extended Drude model agree well.

The independence of $\langle N_{photo} \rangle$ from Sn content in ITO nanocrystals is revealing. This observation indicates that the maximum photodoping level is not determined by competitive Auger recombination dynamics. Instead, it appears to be determined thermodynamically, i.e., by the chemical potentials of the photogenerated carriers. A similar scenario was considered for photodoped ZnO nanocrystals, but kinetic limitations could not be ruled out.[38] This new result can be rationalized as follows: Prior to photodoping, each conduction-band electron within an ITO nanocrystal is compensated by a Sn^{4+} ion in the same nanocrystal. These Sn^{4+} ions stabilize the extra electrons to such an extent that the nanocrystals are not oxidized upon exposure to air. Subsequent photodoping introduces electrons stabilized by charge-compensating protons delivered from the EtOH oxidation reaction. As a consequence, the chemical potentials (V_{photo}) of these photogenerated electrons are essentially the same in all of the nanocrystals, independent of Sn content or initial electron density (Scheme 1).

Three control experiments confirm this interpretation. In the first, the as-prepared 9.0% ITO and In_2O_3 nanocrystals were mixed and the absorption spectra monitored for evidence of electron transfer, which would imply an elevated chemical potential in the ITO nanocrystals. Figure 3a shows the

Scheme 1

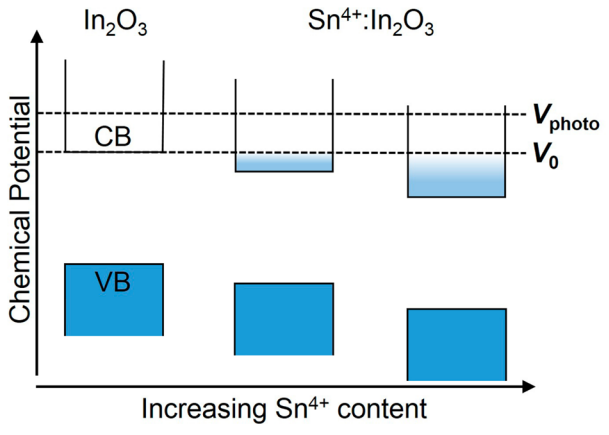

DOI: 10.1021/ja5116953
J. Am. Chem. Soc. 2015, 137, 518−524

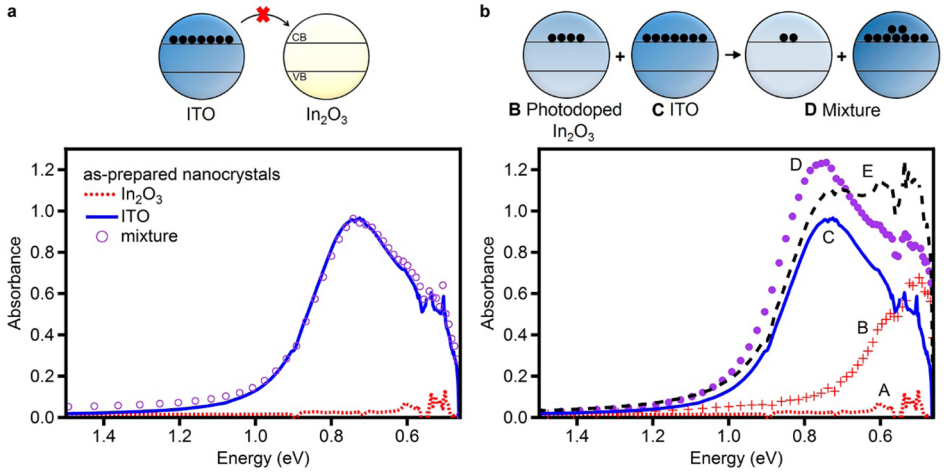

Figure 3. (a) Absorption spectra of as-prepared In_2O_3 nanocrystals (dotted), 9.0% Sn:In_2O_3 nanocrystals (solid), and an anaerobic mixture of the two (circles, both 1 μM in 1:1 toluene/THF). The resulting spectrum shows no indication of electron transfer from the ITO to In_2O_3 nanocrystals. (b) Absorption spectra of: (A) as-prepared In_2O_3 nanocrystals (1 μM in 1:1 toluene/THF with ~3 × 10^5 equiv EtOH, anaerobic); (B) the same nanocrystals after maximal photodoping; (C) as-prepared 9.0% Sn:In_2O_3 nanocrystals;and (D) after adding 1 equiv of maximally photodoped In_2O_3 nanocrystals to a solution of as-prepared 9.0% Sn:In_2O_3 nanocrystals. Spectrum E is a numerical summation of absorption spectra B and C. Spectrum E does not match spectrum D, confirming interparticle electron transfer in mixture of spectrum D.

absorption spectra of as-prepared In_2O_3 and 9.0% Sn:In_2O_3 nanocrystals prepared separately. The absorption spectrum measured after adding the ITO nanocrystals to the In_2O_3 nanocrystals is a simple superposition of the two independent absorption spectra. This result shows that electron transfer from as-prepared ITO nanocrystals to as-prepared In_2O_3 nanocrystals does not occur, and hence that the Fermi level of the ITO nanocrystals is not above the conduction-band edge of the In_2O_3 nanocrystals. In the second experiment, this mixture of as-prepared nanocrystals was photodoped and monitored spectroscopically, with the observation that electrons are added to both types of nanocrystals concurrently (Figure S3). In the third experiment, as-prepared ITO nanocrystals were added to photodoped In_2O_3 nanocrystals (1 equiv) and the absorption spectrum monitored for evidence of electron transfer. The spectrum of this mixture is shown in Figure 3b. It is essentially identical to the spectrum of a mixture of the same nanocrystals after concurrent photodoping, but at roughly half the intensity (Figure S4). This result demonstrates that electrons do indeed transfer between nanocrystals to equilibrate chemical potentials.

Collectively, these results strongly support the alignment of as-prepared nanocrystal chemical potentials (V_0) as depicted in Scheme 1. The picture that emerges is thus that Sn doping does not raise the nanocrystal Fermi level, but instead it stabilizes the band edges relative to external redox couples (or vacuum), as summarized in Scheme 1. Under air-free conditions, irreversible photochemical oxidation of EtOH then raises the electron chemical potential to V_{photo} (Scheme 1), as dictated by the photoredox reaction and the stability of its products. The striking result of Figure 2b is that this increase is independent of the amount of Sn or the number of conduction-band electrons initially within the as-prepared nanocrystals.

With the electron densities of these nanocrystals defined, it is now possible to quantify the effect of Sn on ITO LSPR energies independent of the effects of free carriers. Nanocrystals with different Sn concentrations were photodoped to the same final electron density and their IR LSPRs compared. Figure 4 plots the NIR absorption spectra of three such ITO nanocrystal

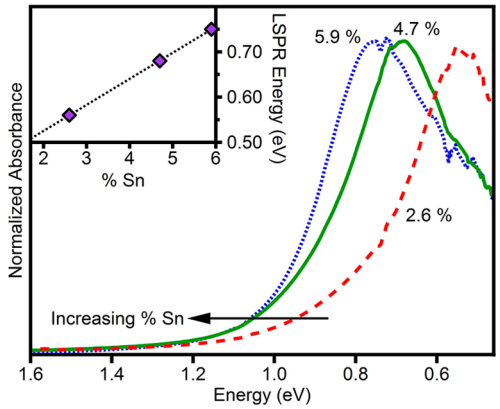

Figure 4. Absorption spectra of ITO nanocrystals with 2.6% (dashed red), 4.7% (solid green), and 5.9% (dotted blue) Sn content, all having the same carrier density of 3.65 × 10^{20} cm^{-3}. Inset: Plot of the LSPR energy versus Sn cation mole fraction (%) at this carrier density.

samples (d = 6.1, 6.8, 6.4 nm; [Sn] = 2.6, 4.7, 5.9%, respectively), all photodoped to the same total electron density of ~3.65 × 10^{20} cm^{-3}. For a fixed carrier density, increasing the Sn content from 2.6 to 5.9% increases the LSPR energy by ~0.2 eV. The inset to Figure 4 plots these LSPR energies as a function of the Sn content and reveals a linear relationship with a slope of 0.06 eV/%Sn. Quantum confinement cannot be responsible for this increase in LSPR energies[46] because these ITO nanocrystals are substantially larger than the electron in In_2O_3. Moreover, the trend in Figure 4 (inset) does not track the small differences in nanocrystal diameter within this series. The change in the high-frequency dielectric constant (ε_∞) also cannot account for the magnitude of this Sn dependence, because the refractive indices of In_2O_3 and SnO_2 are experimentally indistinguishable (1.8–2.0). Instead, this blue shift is attributed to the disruptive impact of Sn on the electronic structure of In_2O_3, in the same way as composition control allows semiconductor band gap engineering. Microscopically, the misalignment of In and Sn empty valence

DOI: 10.1021/ja5116953
J. Am. Chem. Soc. 2015, 137, 518–524

orbitals in ITO causes minima in the In_2O_3 conduction-band wave function amplitudes at each Sn site.

The results presented above thus demonstrate that the LSPR energies of ITO nanocrystals are affected separately by both the number of conduction-band electrons and the number of impurity ions in the nanocrystal: Greater Sn incorporation leads to higher LSPR energies even without introducing more conduction-band electrons. More generally, these data highlight the observation that the relationship between carrier density and LSPR energy frequently invoked in recent literature[1−3,14] is not as straightforward as generally assumed. For example, similar perturbations of the band structure and carrier dynamics must also accompany vacancy formation in plasmonic semiconductors such as $Cu_{2-x}E$ (E = S, Se, Te).[14−16,50,56] Quantitative analysis of the LSPR energies of those semiconductors without accounting for such effects will therefore yield incorrect carrier densities. Even LSPRs generated by redox doping may be affected by perturbations due to the presence of counterions, although such perturbations are likely small compared to those from aliovalent substitution or lattice vacancy formation. This sensitivity of LSPR frequencies to lattice defects, combined with the possibility of strong quantum confinement effects,[46] identifies doped semiconductor nanocrystals as highly flexible platforms for tuning IR plasmons.

Finally, we address the magneto-optical properties of these nanocrystals. Recently, MCD spectroscopy has been demonstrated as a powerful probe of the LSPRs of both metal nanoparticles[57] and electronically doped semiconductor nanocrystals.[46] Large magneto-optical responses have been reported in both classes of plasmonic materials. For high-carrier-density ZnO nanocrystals, the LSPR magneto-optical spectra closely resemble those of metal nanoparticles. To probe the analogous magneto-optical properties of these ITO nanocrystals, low-temperature spectroscopic measurements were performed on 9.0% Sn:In_2O_3 nanocrystals embedded into poly(lauryl methacrylate) (PLMA) matrices as "frozen solutions". The transfer from toluene to PLMA has little effect on the LSPR band (Figure S5). The LSPR absorption spectrum is nearly independent of temperature (Figure S6). Figure 5a plots the absorption spectrum collected at 20 K, and Figure 5b plots variable-field MCD spectra of the same film collected at 1.8 K. As in metal nanoparticles and *n*-type ZnO nanocrystals, the LSPR gives rise to an intense derivative-shaped MCD signal with its crossing point red-shifted slightly from the absorption maximum. The inset of Figure 5b plots relative integrated MCD intensity as a function of magnetic field at 1.8 K. Importantly, this intensity is linear with field and shows no evidence of saturation at high fields, indicating that it does not derive from ground-state Curie paramagnetism. Additionally, the MCD spectrum shows no temperature dependence (Figure S7). The similarities between these data and those of other plasmonic nanocrystals support the proposal[46] that these characteristics (linear field dependence and no temperature dependence) are signatures of LSPRs in doped semiconductor nanocrystals. More specifically, this behavior is reminiscent of Pauli-type paramagnetism observed in metals[58] and is consistent with the classical notion of magnetoplasmonic free-carrier excitations.[57]

CONCLUSION

In summary, photodoping allows the LSPRs of colloidal In_2O_3 and ITO nanocrystals to be tuned post-synthetically. Titration of the photochemically added electrons against mild oxidants allows direct quantification of the carrier densities without relying on models, which may be inaccurate especially at very low carrier densities, under quantum confinement, or for alloyed compositions. Surprisingly, the maximum number of extra electrons that can be added photochemically is largely unaffected by the starting number of electrons introduced via aliovalent doping with Sn^{4+}, suggesting that the maximum number of electrons added photochemically is not limited by competing fast multicarrier Auger recombination processes but is instead determined thermodynamically. By chemical titration of the charge carriers in these nanocrystals, we have been able to separately evaluate the effects of added electrons and added impurity ions on the energies of the LSPRs. The results reveal that the perturbation of the nanocrystal electronic structure by the added impurity is considerable and that the final plasmon energies across a series of ITO compositions are significantly affected by this perturbation. Compositional plasmon engineering can thus be used to tune the energies of LSPRs in doped semiconductor nanocrystals beyond the ranges normally accessible via tunable carrier densities. These findings have broad implications for the analysis of LSPRs in doped semiconductor nanocrystals in general, where until now such effects have not been explicitly separated experimentally. Finally, the observation of strong IR magneto-optical responses arising from these nanocrystal LSPRs bolsters prior analysis of doped ZnO nanocrystal plasmonic magneto-optics and may have interesting ramifications for low-energy plasmonic sensing or imaging technologies.

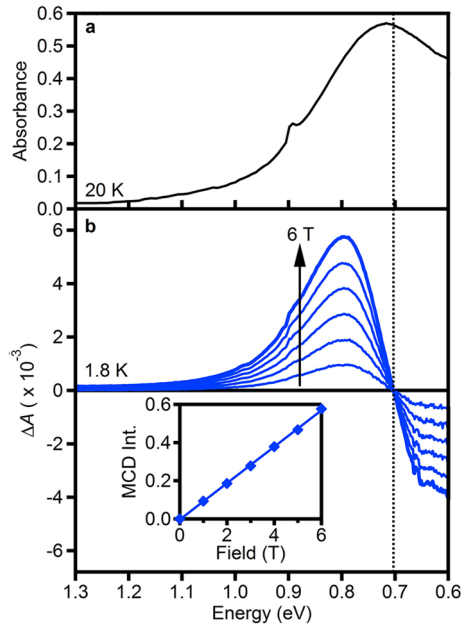

Figure 5. (a) 20 K absorption and (b) 1.8 K variable-field MCD spectra of 9.0% Sn:In_2O_3 nanocrystals in a PLMA matrix. The inset plots the MCD intensity at 1.8 K as a function of applied magnetic field. The solid line is a linear fit to the data.

EXPERIMENTAL METHODS

Chemicals. $[FeCp^*_2][BAr_F]$ ($[FeCp^*_2]^+$ = decamethylferrocenium, $[BAr_F]^-$ = tetrakis[3,5-bis(trifluoromethyl)phenyl]borate) was synthesized following literature procedures.[59] The precursors sodium tetrakis[3,5-bis(trifluoromethyl)phenyl]borate, bis(pentamethylcyclopentadienyl)iron(II), and iron(III) chloride (99.9%) were purchased from Sigma-Aldrich and used without further purification. Ammonium cerium nitrate (98%) was purchased from

DOI: 10.1021/ja5116953
J. Am. Chem. Soc. 2015, 137, 518−524

Sigma-Aldrich and dried under vacuum at 110 °C for ~15 h before use. All oxidants were stored in a N_2 glovebox.

Nanocrystal Synthesis and General Characterization. In_2O_3 and Sn:In_2O_3 nanocrystals were synthesized as reported previously.[43] Nanocrystals were dried, pumped into a N_2 glovebox, and dispersed in toluene for storage. Tri-*n*-octylphosphine oxide (99%) was added to the nanocrystal solutions to aid in colloidal stability during photodoping and titrations. Nanocrystal and dopant concentrations were determined via inductively coupled plasma optical emission spectroscopy using a PerkinElmer Optima 8300. UV−vis near-IR spectra (4.1−0.4 eV) were measured using a Cary 500 spectrometer. IR spectra (1.0−0.1 eV) were measured using a Bruker Vector 33 spectrometer. Nanocrystal diameters were determined via statistical analysis of transmission electron microscope images taken on a JEOL 2100 microscope. All nanocrystals had average diameters of 5.5−6.8 nm.

Photodoping. Dispersions of In_2O_3 or ITO nanocrystals in 1:1 toluene/THF with ~3 × 10^5 equivalents EtOH were prepared anaerobically and loaded into an air-free cuvette with a 2 mm path length. The nanocrystals were photodoped by illumination with a 100 W Hg/Xe Oriel photolysis lamp (~2 W/cm^2, ~1.5 cm illumination diameter) using aqueous $CuSO_4$ to filter out IR photons. Absorption spectra were monitored until the LSPR absorption stopped increasing on the minute time scale, at which point the nanocrystals were considered to be maximally photodoped. The data in Figure 1 were collected using a Bruker Vector 33 IR spectrometer. The nanocrystal solution was loaded into an air-free IR cell with a 50 μm Teflon spacer between two CaF_2 windows.

Determination of Electron Densities. To the photodoped nanocrystals, aliquots of $[FeCp^*_2][BAr_F]$ in THF were added anaerobically and the absorption spectra monitored after each addition. As titrations required larger volume and adequate diffusion, these experiments were conducted in a 2 mm air-free quartz cuvette and measured on a Cary 500 spectrophotometer.

Low-Temperature Absorption and MCD Spectroscopy. A 10 μL aliquot of ~2 μM 9.0% Sn-doped In_2O_3 nanocrystals was added to 50 μL of ~2% PLMA in toluene. The ITO-PLMA solution was evaporated to ~5 μL, sandwiched between two quartz discs, and heated for 2 h at 75 °C. The resulting film had a slightly red-shifted LSPR from that of the colloidal nanocrystals (see Figure S5). For low-temperature absorption measurements, the sample was mounted in a closed-cycle helium refrigerator, and spectra were collected with a Cary 500 spectrometer. For MCD measurements, the film was mounted in a high-field superconducting magneto-optical cryostat (Cryo-Industries SMC-1659 OVT) with a variable-temperature sample compartment oriented in the Faraday configuration. Spectra were measured using an Aviv 40DS spectropolarimeter with an InGaAs detector (Teledyne-Judson).

■ ASSOCIATED CONTENT

Ⓢ Supporting Information

Additional experimental results from ITO oxidation experiments, electron-transfer experiments, and temperature-dependent absorption and MCD measurements. This material is available free of charge via the Internet at http://pubs.acs.org.

■ AUTHOR INFORMATION

Corresponding Authors

gamelin@chem.washington.edu
milliron@che.utexas.edu

Notes

The authors declare no competing financial interest.

■ ACKNOWLEDGMENTS

The authors thank Gerard M. Carroll for valuable discussions. This research was supported by the U.S. National Science Foundation (CHE-1151726 to D.R.G. and Graduate Research Fellowship DGE-1256082 to A.M.S.) and by the U.S. Department of Energy (ARPA-E to D.J.M.). Some of this research was carried out at the Molecular Foundry, Lawrence Berkeley National Laboratory, a user facility supported by the Office of Science, Office of Basic Energy Sciences, of the U.S. Department of Energy under contract no. DE-AC02-05CH11231. D.J.M. acknowledges support of the Welch Foundation (F-1848). The authors gratefully acknowledge additional support from the University of Washington Clean Energy Institute.

■ REFERENCES

(1) Routzahn, A. L.; White, S. L.; Fong, L.-K.; Jain, P. K. *Israel J. Chem.* **2012**, *52*, 983.
(2) Scotognella, F.; Valle, G.; Srimath Kandada, A.; Zavelani-Rossi, M.; Longhi, S.; Lanzani, G.; Tassone, F. *Eur. Phys. J. B* **2013**, *86*, 1.
(3) Comin, A.; Manna, L. *Chem. Soc. Rev.* **2014**, *43*, 3957.
(4) Faucheaux, J. A.; Stanton, A. L. D.; Jain, P. K. *J. Phys. Chem. Lett.* **2014**, *5*, 976.
(5) Lounis, S. D.; Runnerstrom, E. L.; Llordes, A.; Milliron, D. J. *J. Phys. Chem. Lett.* **2014**, *5*, 1564.
(6) Hartland, G. *J. Phys. Chem. Lett.* **2014**, *5*, 1583.
(7) Shim, M.; Guyot-Sionnest, P. *Nature* **2000**, *407*, 981.
(8) Shim, M.; Guyot-Sionnest, P. *J. Am. Chem. Soc.* **2001**, *123*, 11651.
(9) Engel, J. H.; Surendranath, Y.; Alivisatos, A. P. *J. Am. Chem. Soc.* **2012**, *134*, 13200.
(10) Valdez, C. N.; Braten, M.; Soria, A.; Gamelin, D. R.; Mayer, J. M. *J. Am. Chem. Soc.* **2013**, *135*, 8492−8495.
(11) Palomaki, P. K. B.; Miller, E. M.; Neale, N. R. *J. Am. Chem. Soc.* **2013**, *135*, 14142.
(12) Koh, W.-k.; Koposov, A. Y.; Stewart, J. T.; Pal, B. N.; Robel, I.; Pietryga, J. M.; Klimov, V. I. *Sci. Rep.* **2013**, *3*, 2004.
(13) Wheeler, L. M.; Neale, N. R.; Chen, T.; Kortshagen, U. R. *Nat. Commun.* **2013**, *4*, 2197.
(14) Luther, J.; Jain, P.; Ewers, T.; Alivisatos, A. *Nat. Mater.* **2011**, *10*, 361.
(15) Dorfs, D.; Härtling, T.; Miszta, K.; Bigall, N. C.; Kim, M. R.; Genovese, A.; Falqui, A.; Povia, M.; Manna, L. *J. Am. Chem. Soc.* **2011**, *133*, 11175.
(16) Kriegel, I.; Jiang, C.; Rodríguez-Fernández, J.; Schaller, R. D.; Talapin, D. V.; da Como, E.; Feldmann, J. *J. Am. Chem. Soc.* **2011**, *134*, 1583.
(17) Manthiram, K.; Alivisatos, A. *J. Am. Chem. Soc.* **2012**, *134*, 3995.
(18) Kanehara, M.; Koike, H.; Yoshinaga, T.; Teranishi, T. *J. Am. Chem. Soc.* **2009**, *131*, 17736.
(19) Wang, T.; Radovanovic, P. V. *J. Phys. Chem. C* **2011**, *115*, 406.
(20) Buonsanti, R.; Llordes, A.; Aloni, S.; Helms, B. A.; Milliron, D. J. *Nano Lett.* **2011**, *11*, 4706.
(21) Schimpf, A. M.; Ochsenbein, S. T.; Buonsanti, R.; Milliron, D. J.; Gamelin, D. R. *Chem. Commun.* **2012**, *48*, 9352.
(22) De Trizio, L.; Buonsanti, R.; Schimpf, A. M.; Llordes, A.; Gamelin, D. R.; Simonutti, R.; Milliron, D. J. *Chem. Mater.* **2013**, *25*, 3383.
(23) Ye, X.; Fei, J.; Diroll, B. T.; Paik, T.; Murray, C. B. *J. Am. Chem. Soc.* **2014**, *136*, 11680.
(24) Diroll, B. T.; Gordon, T. R.; Gaulding, E. A.; Klein, D. R.; Paik, T.; Yun, H. J.; Goodwin, E. D.; Damodhar, D.; Kagan, C. R.; Murray, C. B. *Chem. Mater.* **2014**, *26*, 4579.
(25) Liang, X.; Ren, Y.; Bai, S.; Zhang, N.; Dai, X.; Wang, X.; He, H.; Jin, C.; Ye, Z.; Chen, Q.; Chen, L.; Wang, J.; Jin, Y. *Chem. Mater.* **2014**, *26*, 5169.
(26) Wang, C. J.; Shim, M.; Guyot-Sionnest, P. *Science* **2001**, *291*, 2390.
(27) Roest, A. L.; Kelly, J. J.; Vanmaekelbergh, D.; Meulenkamp, E. A. *Phys. Rev. Lett.* **2002**, *89*, 036801.
(28) Vanmaekelbergh, D.; Roest, A. L.; Germeau, A.; Kelly, J. J.; Meulenkamp, E. A.; Allan, G.; Delerue, C. *Phys. Rev. Lett.* **2003**, *91*, 169704.

DOI: 10.1021/ja5116953
J. Am. Chem. Soc. 2015, 137, 518−524

(29) Wehrenberg, B. L.; Guyot-Sionnest, P. *J. Am. Chem. Soc.* **2003**, *125*, 7806.
(30) Haase, M.; Weller, H.; Henglein, A. *J. Phys. Chem.* **1988**, *92*, 482.
(31) Wood, A.; Giersig, M.; Mulvaney, P. *J. Phys. Chem. B* **2001**, *105*, 8810.
(32) Liu, W. K.; Whitaker, K. M.; Kittilstved, K. R.; Gamelin, D. R. *J. Am. Chem. Soc.* **2006**, *128*, 3910.
(33) Liu, W. K.; Whitaker, K. M.; Smith, A. L.; Kittilstved, K. R.; Robinson, B. H.; Gamelin, D. R. *Phys. Rev. Lett.* **2007**, *98*, 186804.
(34) Whitaker, K. M.; Ochsenbein, S. T.; Polinger, V. Z.; Gamelin, D. R. *J. Phys. Chem. C* **2008**, *112*, 14331.
(35) Whitaker, K. M.; Ochsenbein, S. T.; Smith, A. L.; Echodu, D. C.; Robinson, B. H.; Gamelin, D. R. *J. Phys. Chem. C* **2010**, *114*, 14467.
(36) Cohn, A. W.; Kittilstved, K. R.; Gamelin, D. R. *J. Am. Chem. Soc.* **2012**, *134*, 7937.
(37) Schrauben, J.; Hayoun, R.; Valdez, C.; Braten, M.; Fridley, L.; Mayer, J. *Science* **2012**, *336*, 1298.
(38) Schimpf, A. M.; Gunthardt, C. E.; Rinehart, J. D.; Mayer, J. M.; Gamelin, D. R. *J. Am. Chem. Soc.* **2013**, *135*, 16569.
(39) Rinehart, J. D.; Schimpf, A. M.; Weaver, A. L.; Cohn, A. W.; Gamelin, D. R. *J. Am. Chem. Soc.* **2013**, *135*, 18782.
(40) Cohn, A. W.; Rinehart, J. D.; Schimpf, A. M.; Weaver, A. L.; Gamelin, D. R. *Nano Lett.* **2014**, *14*, 353−358.
(41) Choi, S.-I.; Nam, K. M.; Park, B. K.; Seo, W. S.; Park, J. T. *Chem. Mater.* **2008**, *20*, 2609.
(42) Gilstrap, R. A.; Capozzi, C. J.; Carson, C. G.; Gerhardt, R. A.; Summers, C. J. *Adv. Mater.* **2008**, *20*, 4163.
(43) Garcia, G.; Buonsanti, R.; Runnerstrom, E. L.; Mendelsberg, R. J.; Llordes, A.; Anders, A.; Richardson, T. J.; Milliron, D. J. *Nano Lett.* **2011**, *11*, 4415.
(44) Lounis, S. D.; Runnerstrom, E. L.; Bergerud, A.; Nordlund, D.; Milliron, D. J. *J. Am. Chem. Soc.* **2014**, *136*, 7110.
(45) Hammarberg, E.; Prodi-Schwab, A.; Feldmann, C. *J. Colloid Interface Sci.* **2009**, *334*, 29.
(46) Schimpf, A. M.; Thakkar, N.; Gunthardt, C. E.; Masiello, D. J.; Gamelin, D. R. *ACS Nano* **2014**, *8*, 1065.
(47) Hayoun, R.; Whitaker, K. M.; Gamelin, D. R.; Mayer, J. M. *J. Am. Chem. Soc.* **2011**, *133*, 4228.
(48) Wang, X.; Jin, Y. Z.; He, H. P.; Yang, F.; Yang, Y. F.; Ye, Z. Z. *Nanoscale* **2013**, *5*, 6464.
(49) Yang, Y. F.; Jin, Y. Z.; He, H. P.; Wang, Q. L.; Tu, Y.; Lu, H. M.; Ye, Z. Z. *J. Am. Chem. Soc.* **2010**, *132*, 13381.
(50) Kriegel, I.; Rodríguez-Fernández, J.; Wisnet, A.; Zhang, H.; Waurisch, C.; Eychmüller, A.; Dubavik, A.; Govorov, A. O.; Feldmann, J. *ACS Nano* **2013**, *7*, 4367.
(51) Mendelsberg, R. J.; Garcia, G.; Li, H.; Manna, L.; Milliron, D. J. *J. Phys. Chem. C* **2012**, *116*, 12226.
(52) Mendelsberg, R. J.; Garcia, G.; Milliron, D. J. *J. Appl. Phys.* **2012**, *111*, 063515.
(53) Hamberg, I.; Granqvist, C. G. *Appl. Phys. Lett.* **1984**, *44*, 721.
(54) Hamberg, I.; Granqvist, C. G. *J. Appl. Phys.* **1986**, *60*, R123.
(55) Gerlach, E. *J. Phys. C: Solid State Phys.* **1986**, *19*, 4585.
(56) Xie, Y.; Riedinger, A.; Prato, M.; Casu, A.; Genovese, A.; Guardia, P.; Sottini, S.; Sangregorio, C.; Miszta, K.; Ghosh, S.; Pellegrino, T.; Manna, L. *J. Am. Chem. Soc.* **2013**, *135*, 17630.
(57) Pineider, F.; Campo, G.; Bonanni, V.; Fernandez, C. J.; Mattei, G.; Caneschi, A.; Gatteschi, D.; Sangregorio, C. *Nano Lett.* **2013**, *13*, 4785.
(58) Kondo, J.; Koikegami, S. *The Physics of Dilute Magnetic Alloys*; Cambridge University Press: Cambridge, 2012.
(59) Le Bras, J.; Jiao, H.; Meyer, W. E.; Hampel, F.; Gladysz, J. A. *J. Organomet. Chem.* **2000**, *616*, 54.

DOI: 10.1021/ja5116953
J. Am. Chem. Soc. 2015, 137, 518−524